



Numerical study on preheating process of molten salt tower receiver in windy conditions

Yuhang Zuo, Yawei Li, Hao Zhou*

State Key Laboratory of Clean Energy Utilization, Institute for Thermal Power Engineering, Zhejiang University, Hangzhou, 310027, China

ARTICLE INFO

Article history:

Received 13 September 2021

Received in revised form

2 March 2022

Accepted 30 March 2022

Available online 5 April 2022

Keywords:

Concentrating solar power

Molten salt tower receiver

Preheating process

Windy condition

Thermal stress

ABSTRACT

In the preheating process of the molten salt tower receiver, the thermal stress is large and the over-temperature problem is prone to occur. The finite volume method and two-dimensional thermoelastic method are combined in this paper to study the preheating process of the receiver tube in windy conditions. The experimental results of a lab-scale receiver verify the numerical model. Then, the influence of heat flux, wind speed, wind direction, ambient temperature and uniformity of heat flux distribution on the preheating process is explored. Finally, the influence of salt filling temperature and salt filling mass flow on the salt circulating is also revealed. The results indicate that the increase in heat flux, decrease in wind speed and increase in ambient temperature decrease the preheating time. The wind in the direction of 30° from the front side of the tube has the greatest influence on the preheating process. Compared with the no-wind condition, the preheating time increases by 177.5%. The maximum tube wall temperature and thermal stress are significantly higher under non-uniform heat flux distribution than those under uniform heat flux distribution. The salt inlet temperature and salt inlet mass flow respectively affect the stable value and reduction rate of thermal stress.

© 2022 Elsevier Ltd. All rights reserved.

1. Introduction

Tower concentrating solar power (CSP) plant with molten salt as heat transfer/storage medium is one of the most promising renewable energy power generation technologies for its ability to solve the intermittent and fluctuating issues of renewable energy [1]. For the most popular two-tank molten salt tower CSP plant, its components include the heliostat field, central receiver, cold and hot salt tank and power generation device. Among them, the central receiver, which occupies 20% of the investment cost of the plant, is mainly responsible for converting the solar radiation concentrated from the heliostat field into the heat of molten salt inside it. Thus, the central receiver is very key to the efficient and safe operation of the plant [2].

During the normal operation of the tower CSP plant, the front side of the receiver always bears a highly non-uniform heat flux. As a result, the overheating problem and fatigue failure are the key challenges faced by the receiver. Yu et al. [3] developed and verified a numerical model of an external cylindrical receiver, and then

carried out a parameter analysis on the thermal performance of the receiver. Albarbar et al. [4] studied the effect of structural parameters on the receiver performance and optimized the receiver design. The result indicated that the thermal efficiency of the optimized receiver increased by about 1%. Xu et al. [5] studied and revealed the dynamic temperature evolution of the heat transfer fluid of the receiver under the change of key parameters. Qaisrani et al. [6] numerically studied the heat loss characteristics of a rectangular external receiver under different wind conditions and proposed an effective design of adding a wind blocking to strengthen the receiver's thermal insulation. Cagnoli et al. [7] investigated the convective heat loss of a billboard-type sodium-cooled receiver at different wind speeds and directions by CFD method, and successfully developed a system-level dynamical model for the receiver with the help of CFD results. Rodríguez-Sánchez et al. [8] comprehensively analyzed an external cylindrical receiver from the thermal, mechanical and hydrodynamic aspects, and found that a compromise between different variables was required to make the receiver performance best. Cantone et al. [9] found that a single-sided heated tube with spiral fins could significantly decrease the peak tube wall temperature compared to a smooth tube. Due to the long-term non-uniform incident flux, the central receiver is prone to plastic deformation and fatigue failure

* Corresponding author.

E-mail address: zhouhao@zju.edu.cn (H. Zhou).

due to thermal stress. Du et al. [10] studied the thermal stress distribution of a single receiver tube, and found that the stress distribution is consistent with the temperature difference between the inner and outer walls. Qaisrani et al. [11] analyzed the axial thermal stress distribution of a receiver tube. And it was found that the equivalent thermal stress would exceed the yield strength of the tube when the safety factor < 2.5 . Zhou et al. [12] modeled and analyzed the variation of thermal stress of an external cylindrical receiver with time on the spring equinox. The results indicated that the peak thermal stress of the receiver at 18:00 was only 53.26% of that at 12:00. Wang et al. [13] studied the influence of tube material on the thermal stress of a tubular receiver, and found that the copper tube had the lowest stress failure ratio. Logie et al. [14] explored the sensitivity of the thermal stress of a non-axisymmetric heated tube to the fluid properties. When the fluid in the tube changed from molten salt to liquid sodium, the peak thermal stress was reduced by 35%. Montoya et al. [15] found that the circumferential distribution of the tube wall temperature was responsible for most stress, and the tube clip significantly increased the thermal stress.

For tower CSP plants, the most widely used molten salt is Solar Salt with a melting point of about 220°C [16]. To reduce heat loss, the molten salt in the receiver needs to be drained at night, and the salt will be refilled during the day. To ensure that there is no solidification and blockage of molten salt when filling, the receiver must be preheated. During the preheating, a subset of the heliostat field is used to provide an evenly distributed axial heat flux of $12\text{--}36\text{ kW/m}^2$ [17]. The goal of the preheating is to make the temperature of the receiver tube higher than the melting point of the molten salt. However, the air in the tube during the preheating process is poor in thermal conductivity, so the temperature of the light-receiving side is always higher than that of the backlight side. To prevent overheating of the receiver, the tube wall temperature is usually limited. Vant-Hull [17] points out that the tube wall should be preheated to $260\text{--}382^{\circ}\text{C}$. Mehos et al. [18] suggest that it should be $340\text{--}375^{\circ}\text{C}$. In addition, the tube has a large circumferential temperature gradient and high thermal stress during the preheating process, which is likely to cause safety problems. Lu et al. [19,20] numerically investigated the dynamical and thermal performance of a tube during salt filling. Vant-Hull et al. [17] introduced the preheating process and preheating algorithm of Solar Two plant under various conditions. Fernandez-Torrijos et al. [21,22] and Perez-Alvarez et al. [23] numerically and experimentally explored the thermal stress of a receiver tube under different conditions during preheating. The results indicated that enhancing heat transfer within the receiver tube (molten salt circulation) and reducing heat flux into the receiver tube (increasing wind speed) both reduced the tube temperature gradient and thus reduced the thermal stress. Wan et al. [24] numerically studied the thermal stress and thermal fatigue of boiling plate in a water/steam cavity receiver during cold start-up. It was found that non-uniform stress and strain would cause the boiling plate to warp. Hefni [25] numerically evaluated the risk of crystallization of molten salt in the receiver tube when the tube was drained, and found that when the salt inlet temperature was 254.84°C , there was a risk of crystallization in the salt circuit. Yang et al. [26] built a high-temperature sodium flat heat pipe receiver, and experimentally studied the startup process. The results indicated that the receiver has good start-up performance.

In summary, the research on the preheating process of molten salt tower receivers under windy conditions is quite lacking. To fill the gap, the finite volume method (FVM) and two-dimensional thermoelastic analytical method were combined in this paper to study the evolution characteristics of the temperature and stress of the receiver tube during preheating and salt circulating under

windy conditions. First, the wall temperature distribution on the tube was obtained by the FVM method, and then the thermal stress distribution and evolution were obtained based on the two-dimensional thermoelastic analytical method. The influence of heat flux, wind speed, wind direction, ambient temperature and uniformity of heat flux distribution on the preheating process was explored. And wall temperature and thermal stress evolutions under different salt inlet temperatures and salt inlet mass flow during salt circulation were also studied. A preheating experiment of the lab-scale receiver was conducted to verify the FVM model, and the experimental results were in good agreement with the simulation results. The work in this paper contributes to understanding the preheating process of the receiver and provides a beneficial data reference for the preheating of the on-site receiver.

2. Methodology

2.1. Receiver description

To study the preheating process, the receiver of a 50 MWe molten salt tower CSP plant was selected as the research object. The receiver is responsible for receiving and converting the solar radiation to heat from the heliostat field composed of 4400 heliostats with a surface area of 138 m^2 . The molten salt used in the plant is the most widely used Solar Salt ($60\text{ wt\% NaNO}_3 + 40\text{ wt\% KNO}_3$). As shown in Fig. 1, the receiver includes 24 heat-absorbing panels, each of which contains 32 tubes with a height of 14 m. The receiver is divided into two parallel molten salt circuits, and each circuit includes 12 panels. After flowing through each circuit, the molten salt is heated. Under the design conditions, the molten salt enters into the receiver at 298°C and flows out at 565°C . The receiver tube is made of Haynes 230, and the related parameters are shown in Table 1.

2.2. The FVM model

The commercial CFD software ANSYS Fluent 16.1 was used to conduct the preheating process simulation of the receiver, and the FVM is used to discretize and solve the governing equations. Considering the computing resources, only a single receiver tube was simulated. The computational domain of the simulation model is presented in Fig. 2(a), which includes three parts: the receiver tube, the fluid inside the tube, and the fluid outside the tube. The fluid inside the tube is the air during preheating and molten salt during salt filling. The fluid flow in the simulation was handled with the Standard $k\text{--}\epsilon$ model, and the fluid flow near the wall was solved with the enhanced wall treatment. As for the radiation during the preheating process, The Discrete Ordinates model was pretty suitable. The SIMPLE algorithm was selected to perform the coupled solution of pressure and velocity in the flow field.

To obtain reasonable calculation results, some boundary conditions need to be defined properly. As shown in Fig. 2(b), the heat flux level was applied to the half circumference of the receiver tube outer wall to simulate the actual solar radiation. For on-site receivers, the axial heat flux distribution is required to be as evenly distributed as possible during preheating [17]. On the one hand, it can prevent safety accidents from uneven heating of the tube. On the other hand, it can also ensure that the preheating speed of each position of the receiver is consistent, so as to avoid frequent adjustment of the heliostat field, which will prolong the preheating time and increase the operating cost of the plant. In addition, due to the small size of a single receiver tube, considering the uniform circumferential distribution of the heat flux on the light-receiving side has little effect on the calculation results. Therefore, the heat flux was assumed to be evenly distributed in the axial and

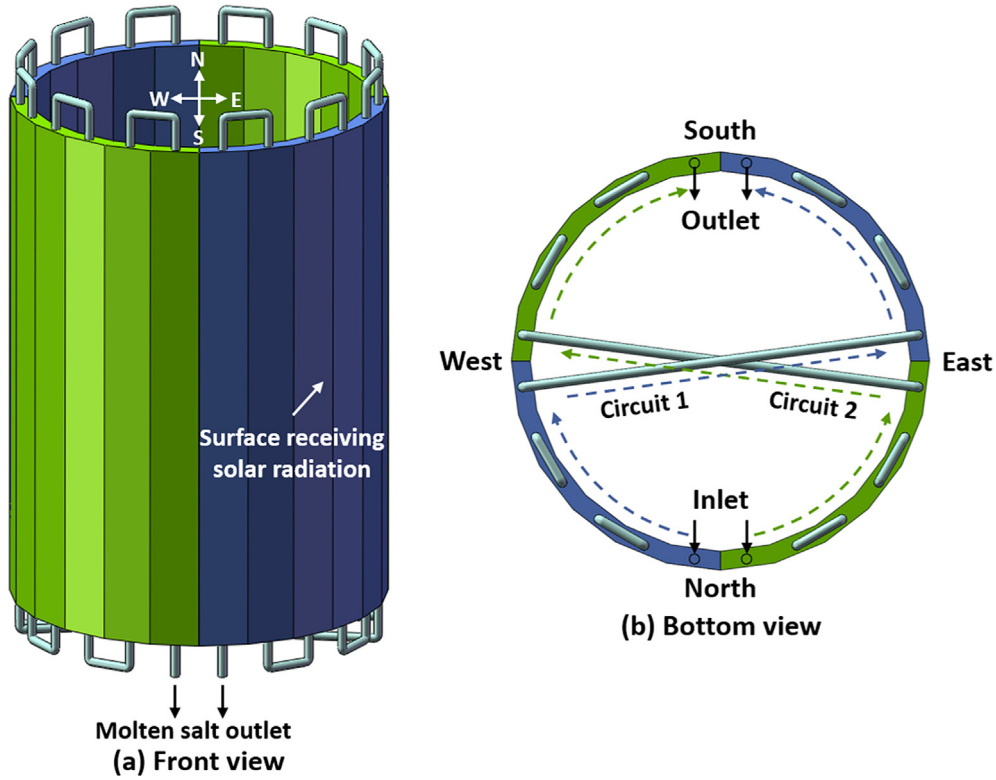


Fig. 1. Schematic of the receiver.

Table 1
Parameters of receiver tube.

Parameter	Value
Diameter (mm)	50.8
Tube wall thickness (mm)	1.5
Tube height (mm)	14,000
Density (kg/m ³)	8890
Specific heat (J/(kg.K))	$308.81 + 0.247 \times T$
Thermal conductivity (W/(m.K))	$2.937 + 0.02 \times T$
Poisson's ratio	0.3
Linear thermal expansion coefficient (K ⁻¹)	12.25×10^{-6}
Young's modulus (GPa)	203

circumferential directions in this work. The mass flow inlet and pressure outlet were applied to the inlet and outlet of the tube, respectively. The adiabatic wall with an emissivity of 0.2 was applied to the wall behind the tube to restore the rear panel behind the on-site receiver [27]. To conduct the simulation under different wind conditions, the velocity inlet was applied to the left surface and the front left half surface of the tube, and the pressure outlet was applied to the right surface and the front right half surface of the tube. The wind from different directions was obtained by synthesizing the vectors of two velocity inlets. The absorptivity of the tube wall coating and emissivity of the tube were set to 0.93 and 0.87, respectively [27]. To ensure the calculation accuracy and reduce the calculation resources, a grid with 845,600 cells was adopted. Fig. 2(c) shows the grid structure around the tube cross section. Table 2 lists all the simulation cases, and the wind direction is illustrated in Fig. 2(d). Notably, the Wind inlet_1 and Wind outlet_2 were respectively changed to the velocity inlet and pressure outlet when the wind direction was 90°.

2.3. The 2D thermoelastic analytical model

At present, one-dimensional and two-dimensional thermoelastic methods are widely used to calculate the thermal stress of hollow cylindrical tubes. The latter considers the contribution of radial and circumferential temperature gradients to thermal stress, while the former only considers the contribution of radial temperature gradient [14,28]. During the preheating process, due to the air with low thermal conductivity in the tube, the circumferential temperature gradient is much larger than the radial temperature gradient. If the one-dimensional method is used, the thermal stress of the tube wall will be seriously underestimated. Thus, the two-dimensional thermoelastic method proposed by Logie et al. [14] was adopted to obtain the thermal stress.

To use the two-dimensional method, the Fourier polynomial method is used to fit the circumferential distribution of the inner and outer wall temperature of the tube. In the equations, only the term of $n = 1$ contributes to the generation of thermal stress.

$$T_i = \bar{T}_i + \sum_{n=1}^{\infty} B'_n \cos n\theta + D'_n \sin n\theta \quad (1)$$

$$T_o = \bar{T}_o + \sum_{n=1}^{\infty} B''_n \cos n\theta + D''_n \sin n\theta \quad (2)$$

In the above equations, \bar{T}_i and \bar{T}_o represent the average inner wall temperature and average outer wall temperature, respectively. And they can be expressed as the following equations.

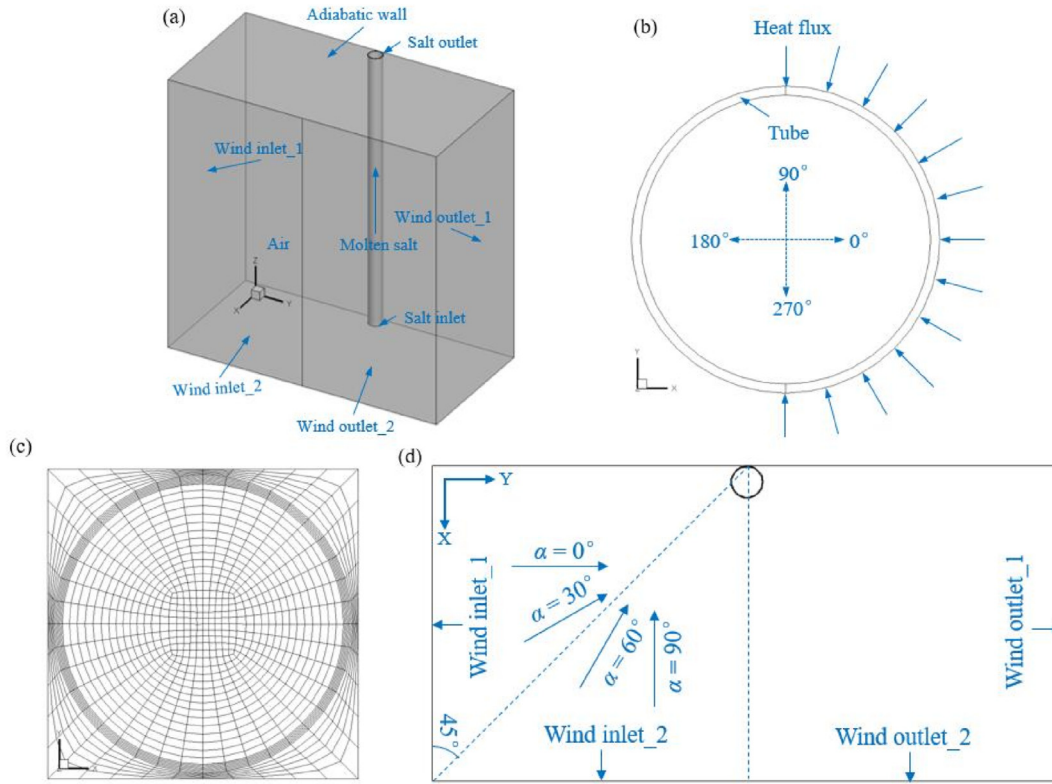


Fig. 2. (a) Schematic of computational domain; (b) Schematic of heat flux loading; (c) Grid of cross section near receiver tube; (d) Schematic of wind direction.

Table 2

Simulation cases.

	Case	Heat flux (kW/m ²)	Wind speed (m/s)	Wind direction (°)	Ambient temperature (°C)	Inlet salt temperature (°C)	Inlet salt mass flow (kg/s)
Without salt circulating	Case_1	10	0	—	20	—	—
	Case_2	20	0	—	20	—	—
	Case_3	30	0	—	20	—	—
	Case_4	40	0	—	20	—	—
	Case_5	30 (Uniform heat flux distribution: q_1)	1.5	0	20	—	—
	Case_6	30	3.0	0	20	—	—
	Case_7	30	4.5	0	20	—	—
	Case_8	30	4.5	30	20	—	—
	Case_9	30	4.5	60	20	—	—
	Case_10	30	4.5	90	20	—	—
	Case_11	30	4.5	0	0	—	—
	Case_12	30	4.5	0	−20	—	—
	Case_13	30	4.5	0	40	—	—
	Case_14	Non-uniform heat flux distribution: q_2	1.5	0	20	—	—
	Case_15	Non-uniform heat flux distribution: q_3	1.5	0	20	—	—
With salt circulating	Case_16	30	1.5	0	20	300	4
	Case_17	30	1.5	0	20	400	4
	Case_18	30	1.5	0	20	500	4
	Case_19	30	1.5	0	20	300	1
	Case_20	30	1.5	0	20	300	2

$$\bar{T}_i = \frac{1}{2\pi} \int_0^{2\pi} T_i d\theta$$

(3)

$$\bar{T}_o = \frac{1}{2\pi} \int_0^{2\pi} T_o d\theta$$

(4)

To calculate the axial thermal stress, the circumferential wall temperature variation expression of the tube cross section is required, which can be defined by Eq. (5).



Fig. 3. Experimental system.

Table 3

Parameters of lab-scale receiver tube.

Parameter	Value
Diameter (mm)	21
Tube wall thickness (mm)	1.2
Tube height (mm)	400
Density (kg/m)	8440
Specific heat (J/(kg.K))	430
Thermal conductivity (W/(m.K))	12.1
Poisson's ratio	0.308
Linear thermal expansion coefficient (K ⁻¹)	12.3 × 10 ⁻⁶
Young's modulus (GPa)	205

$$T_{\theta} = T - (\bar{T}_i - \bar{T}_o) \frac{\ln \frac{r_o}{r}}{\ln \frac{r_o}{r_i}} - \bar{T}_o \quad (5)$$

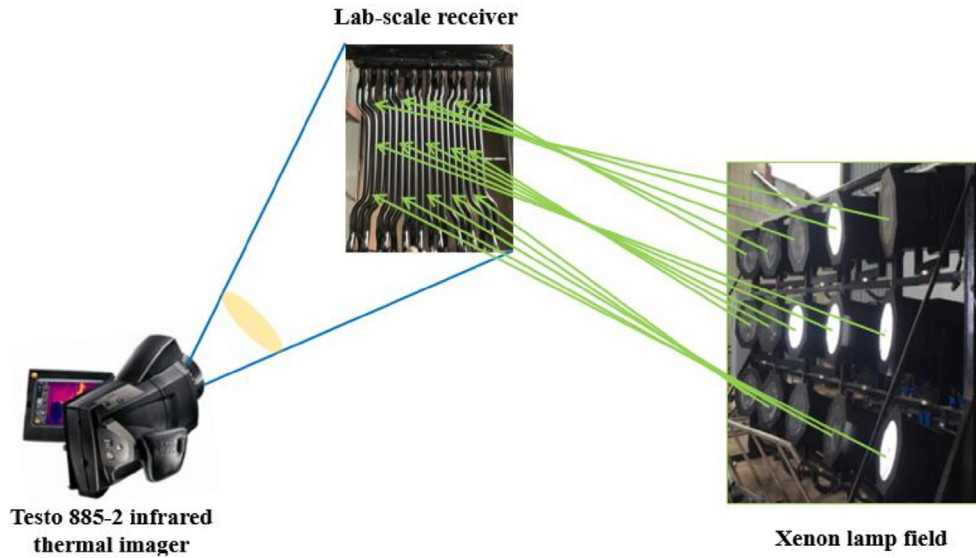
Assuming that the tube is axially limited, zero axial stress and no external mechanical load, all component thermal stresses can be expressed as the following equations.

$$\sigma_r = K \frac{\lambda E}{2(1-\nu)} \left[-\ln \frac{r_o}{r} - \frac{r_i^2}{r_o^2 - r_i^2} \left(1 - \frac{r_o^2}{r^2} \right) \ln \frac{r_o}{r_i} \right] + K_{\theta} \frac{\lambda E}{2(1-\nu)} \left(1 - \frac{r_i^2}{r^2} \right) \left(1 - \frac{r_o^2}{r^2} \right) \quad (6)$$

$$\sigma_{\theta} = K \frac{\lambda E}{2(1-\nu)} \left[1 - \ln \frac{r_o}{r} - \frac{r_i^2}{r_o^2 - r_i^2} \left(1 + \frac{r_o^2}{r^2} \right) \ln \frac{r_o}{r_i} \right] + K_{\theta} \frac{\lambda E}{2(1-\nu)} \left(3 - \frac{r_i^2 + r_o^2}{r^2} - \frac{r_i^2 r_o^2}{r^4} \right) \quad (7)$$

$$\sigma_z = K \frac{\lambda E}{2(1-\nu)} \left[1 - 2 \ln \frac{r_o}{r} - \frac{2r_i^2}{r_o^2 - r_i^2} \ln \frac{r_o}{r_i} \right] + K_{\theta} \frac{\lambda E \nu}{1-\nu} \left(2 - \frac{r_i^2 + r_o^2}{r^2} \right) - \lambda E T_{\theta} \quad (8)$$

In the above equations, K and K_{θ} reflect the contribution of $n = 0$ term and $n = 1$ term to thermal stress, respectively. They can be



(a) The experimental setup.



(b) The main equipment of the experiment.

Fig. 4. The experimental system.

calculated by Eqs. (9) and (10). Where the B'_1 , D'_1 , B''_1 and D''_1 are taken from the coefficients in Eqs. (1) and (2).

$$K = \frac{\overline{T_i} - \overline{T_o}}{\ln \frac{r_o}{r_i}} \quad (9)$$

$$K_\theta = \frac{r r_i r_o}{r_o^2 - r_i^2} \left[\left(\frac{B'_1 r_o - B''_1 r_i}{r_i^2 + r_o^2} \right) \cos \theta + \left(\frac{D'_1 r_o - D''_1 r_i}{r_i^2 + r_o^2} \right) \sin \theta \right] \quad (10)$$

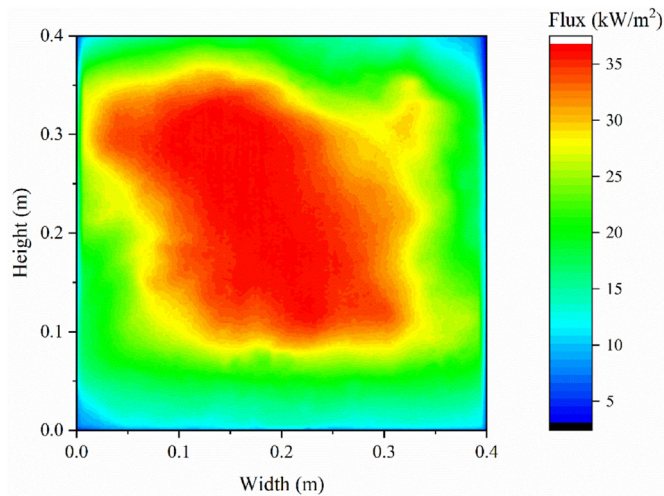


Fig. 5. The heat flux distribution on the receiver surface.

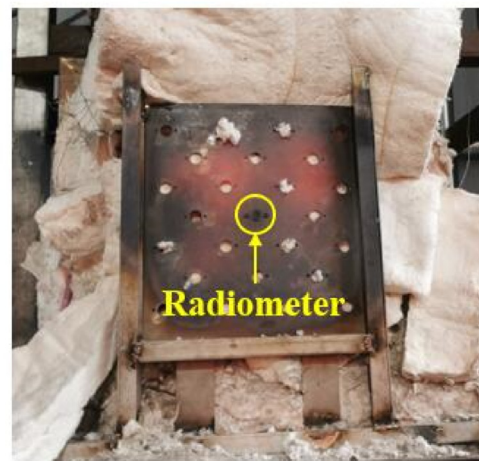
3. Model validation

3.1. Lab-scale receiver

To verify the model, the preheating experiment of a lab-scale receiver was conducted. The whole experiment system includes four parts: xenon lamp group, hot and cold molten salt tank, receiver and steam generator. As shown in Fig. 3, the xenon lamp group composed of 15 xenon lamps with a maximum power of 10 kW is used to simulate the solar radiation received by the receiver, and its power is adjustable. The xenon lamp can be rotated in both horizontal and vertical directions. The receiver includes 6 panels, and there are 3 tubes in each panel. The tube material is Inconel 625, and the outer wall of each pipe is coated with black Pyromark 2500. The effective receiving surface size of the receiver is 400 mm × 400 mm. Table 3 presents the parameters of the receiver tube.



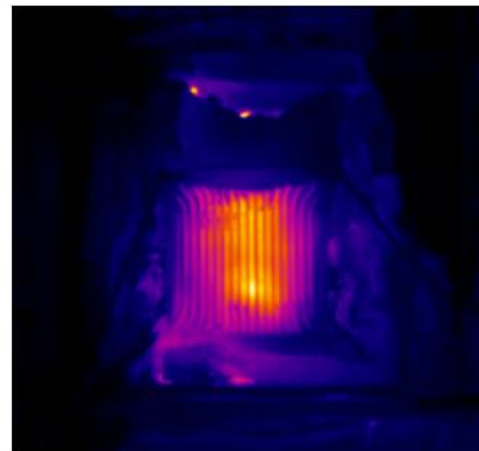
(a) Lambert plate



(b) Radiometer



(c) Preheating experiment



(d) Photo taken by the infrared thermal imager

Fig. 6. Preheating experiment site.

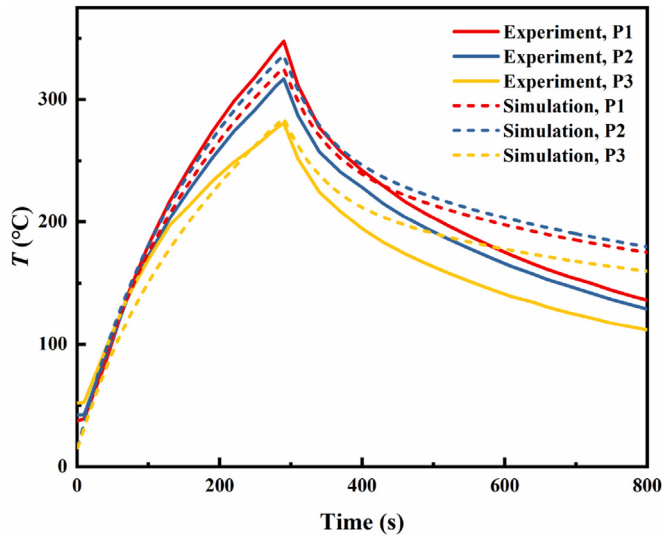


Fig. 7. Model validation.

3.2. Experimental method

The temperature distribution on the receiver is directly related to the incident heat flux distribution. Thus, to prevent excessive thermal stress of the receiver during preheating, the incident heat flux distribution should be adjusted to be as uniform as possible. As a result, we first adjusted the direction of 15 xenon lamps before the experiment. After that, the power of each xenon lamp was adjusted to about 2 kW. Once the receiver received the radiation of 15 xenon lamps, the tube wall temperature increased. The Testo 885-2 infrared thermal imager with a temperature range of 1200 °C and a measurement error of ± 0.03 °C was applied to measure the temperature distribution on the receiver's front side. In the experiment, when the maximum temperature of the receiver reached 350 °C, the 15 xenon lamps were quickly turned off, the experiment stopped, and then the receiver cooled naturally.

To conduct the simulation and compare with the experimental results, the heat flux distribution on the receiver surface must be

measured. This work was accomplished by combining the Lambert plate, CCD camera and radiometer. The Lambert plate and CCD camera were responsible for obtaining the relative distribution of heat flux, while the radiometer was used to measure the actual heat fluxes at several points. In this way, the actual heat flux distribution of the entire surface was obtained. The method of heat flux measurement was illustrated in detail in the literature [29] and literature [30].

The experimental setup and main equipment are shown in Fig. 4. The measured heat flux on the receiver surface is shown in Fig. 5. The maximum and minimum heat fluxes are 36.8 kW/m² and 3.1 kW/m², respectively. The heat flux distribution in the center is generally uniform, while the heat flux at the edge is small. Fig. 6 shows some photos during the experiment.

3.3. Model validation

The second tube on the third panel of the lab-scale receiver was selected as the simulation object. The absorptivity and emissivity of the tube were set to 0.93 and 0.87, respectively. The simulation and experiment results of the three points P1, P2 and P3 in Fig. 3 (c) were selected for comparison. As shown in Fig. 7, in the preheating stage, the temperature evolution trends at the three points obtained by simulation and experiment are pretty consistent, and the maximum deviations at the three points are 6.2%, 6.2% and 1.6%, respectively. After the preheating, the receiver begins to cool naturally. At this stage, the wall temperature decreases significantly faster in the experiment than that in the simulation. The reason for the above phenomenon is that in the preheating stage and natural cooling stage, the tube wall temperature mainly depends on the heat flux and ambient temperature respectively. In the preheating stage, the heat flux in the simulation is similar to that in the experiment, so the temperature evolution trends are consistent. In the natural cooling stage, the receiver tube is in a large semi-open space and a closed space in the experiment and simulation, respectively. After removing the heat flux, the air temperature around the receiver tube decreases rapidly during the experiment and slowly during the simulation, so the wall temperature in the experiment decreases significantly faster than that in the simulation. In general, the FVM model is reliable to obtain the receiver

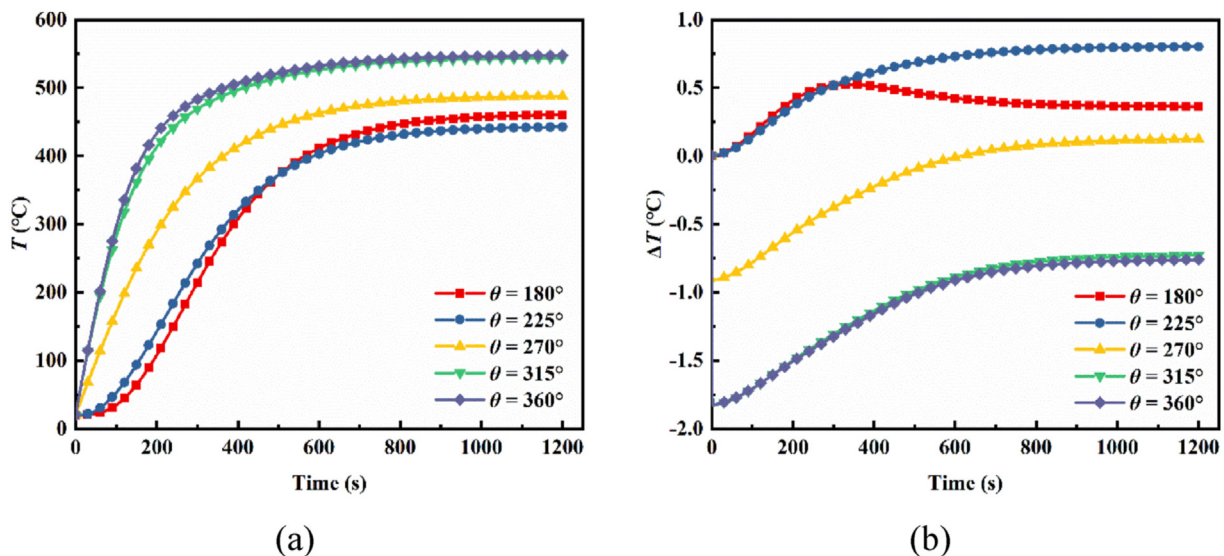


Fig. 8. (a) Outer wall temperature evolutions at different circumferential positions; (b) Differences between inner wall temperature and outer wall temperature at different circumferential positions. ($q = 30$ kW/m², $v = 0$ m/s, $T_{\text{amb}} = 20$ °C).

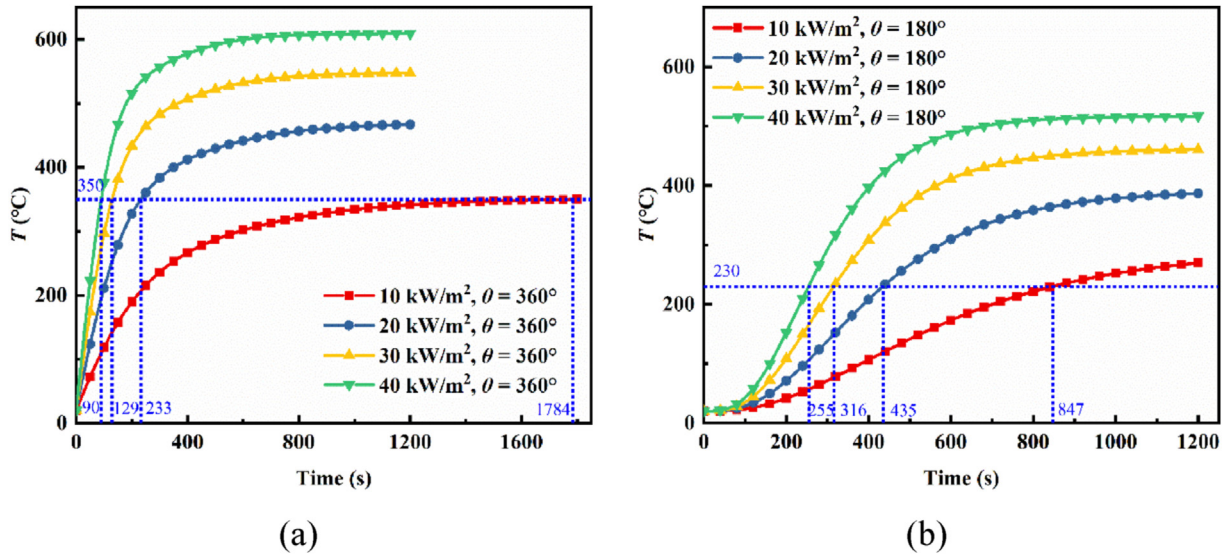


Fig. 9. Tube wall temperature evolutions under different heat fluxes. (a) The maximum wall temperature point; (b) the minimum wall temperature point.

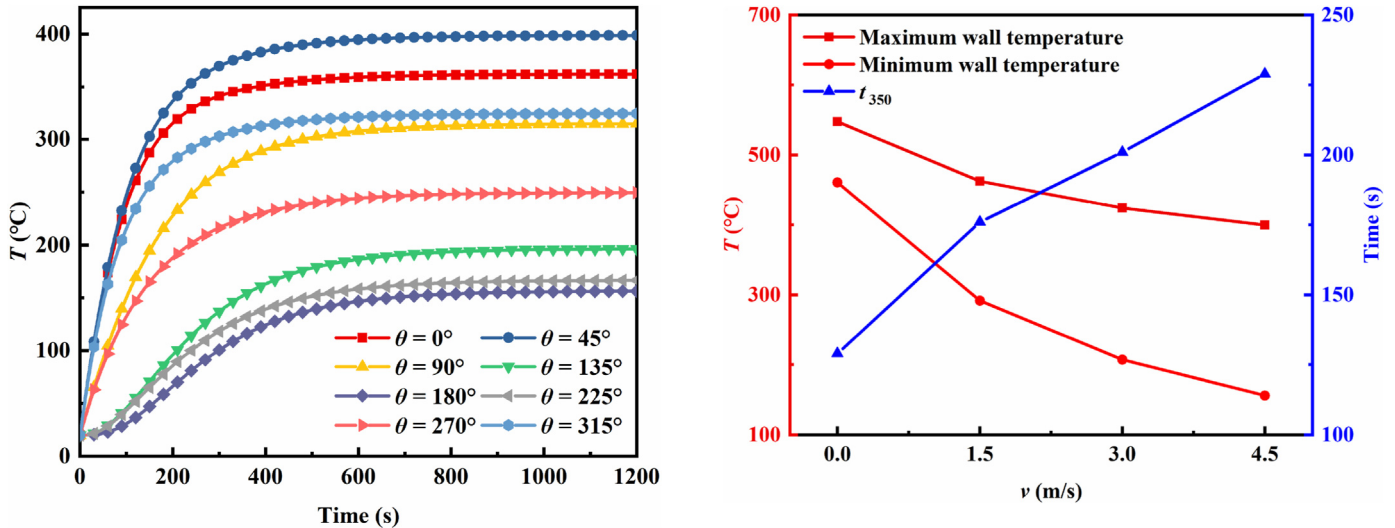


Fig. 10. Outer wall temperature evolutions at different circumferential positions. ($q = 30 \text{ kW/m}^2$, $v = 4.5 \text{ m/s}$, $\alpha = 0^\circ$, $T_{\text{amb}} = 20^\circ \text{C}$).

Fig. 11. Effect of wind speed on preheating process.

tube wall temperature of the preheating process.

4. Results and discussion

4.1. Tube wall temperature

4.1.1. Effect of heat flux on tube wall temperature

Since the heat flux is uniformly distributed in the axial direction, so only the section $z = 7.0 \text{ m}$ is analyzed. The heat flux has a great influence on the preheating effect of the receiver. Fig. 8(a) shows the evolutions of the outer wall temperature at different circumferential positions when the heat flux $q = 30 \text{ kW/m}^2$ under no wind. During the preheating process, the tube wall temperature limited range is considered to be 230–350 °C. In this temperature range, the maximum and minimum wall temperatures appear at $\theta = 360^\circ$ and $\theta = 180^\circ$, respectively. After the preheating starts, the tube wall temperature rises rapidly. Since the tube front side is loaded with the heat flux, and the back side is mainly heated by the

heat conduction and the heat radiation of the tube front side, the temperature rise rate of the front side is significantly higher than that of the back side. When the preheating is stable, the wall temperature at $\theta = 180^\circ$, $\theta = 225^\circ$, $\theta = 270^\circ$, $\theta = 315^\circ$ and $\theta = 360^\circ$ are 460.6 °C, 442.8 °C, 487.9 °C, 543.8 °C and 547.6 °C, respectively. As shown in Fig. 8(b), the difference between the inner wall temperature and outer wall temperature at each circumferential position does not exceed 2 °C during the whole preheating process. This is caused by the poor thermal conductivity of the air inside the tube and the good thermal conductivity of the tube.

The on-site receiver usually needs to be preheated quickly, so the preheating time is key for the preheating process. Here, the time when the maximum wall temperature of the tube reaches 350 °C t_{350} and the time when the minimum wall temperature reaches 230 °C t_{230} are defined to represent the preheating time. As shown in Fig. 9, the preheating time significantly decreases with the increase of the heat flux. As the heat flux increases from 10 kW/m^2 to 40 kW/m^2 , t_{350} and t_{230} decreased from 1784 s to 847 s–90 s and 255 s, respectively, a decrease of 95.0% and 69.9%, respectively. Notably, when the heat flux is 10 kW/m^2 , t_{230} is smaller than t_{350} ,

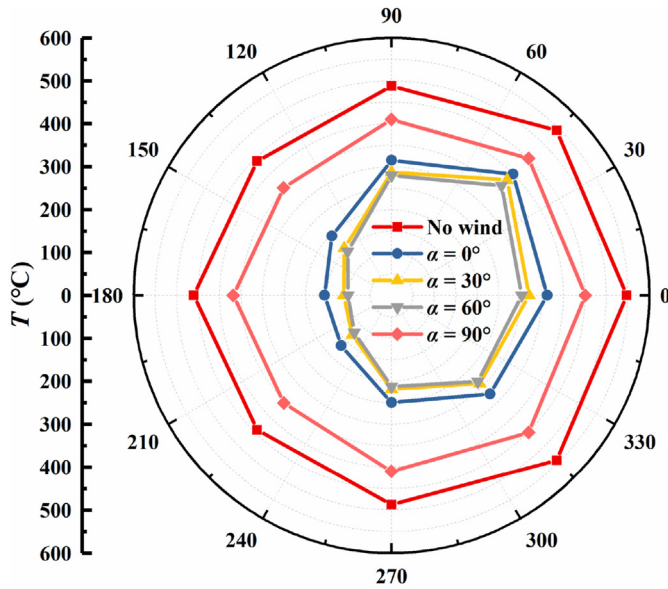


Fig. 12. Circumferential distributions of outer wall temperature under different wind directions when preheating process is stable.

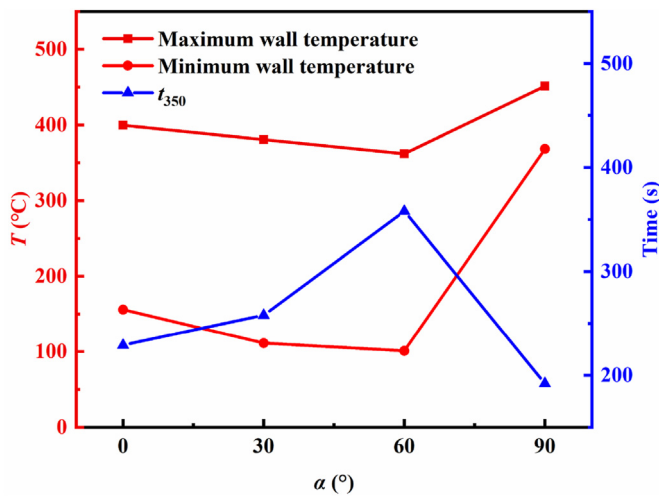


Fig. 13. Effect of wind direction on preheating process.

which means that the tube can be successfully preheated by directly loading a constant heat flux. While t_{230} is significantly larger than t_{230} under the other heat fluxes. This is, it is necessary to repeatedly reduce and increase the heat flux in relevant areas for preheating according to the tube wall temperature in these cases.

4.1.2. Effect of wind speed on tube wall temperature

Fig. 10 presents the outer wall temperature evolutions at different circumferential positions when the wind direction $\alpha = 0^\circ$ and wind speed $v = 4.5$ m/s. Due to the wind, the temperature distribution of the tube wall is no longer symmetrical, and the wall temperature on the windward side ($\theta = 180^\circ - 360^\circ$) is lower than the leeward side ($\theta = 0^\circ - 180^\circ$). And the maximum wall temperature point changes from $\theta = 360^\circ$ to $\theta = 45^\circ$. Besides, the minimum wall temperature cannot reach 230°C under the current heat flux. The maximum and minimum wall temperatures after the preheating process are stable is shown in Fig. 11, they both decrease with the increase of the wind speed. From 0 m/s to 4.5 m/s, the

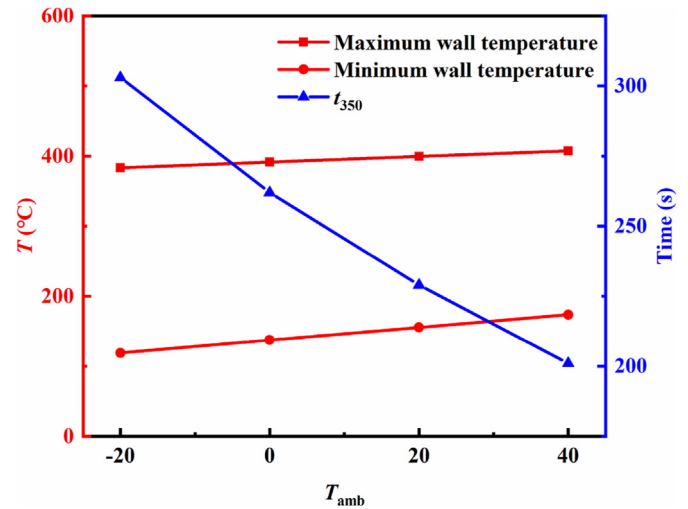


Fig. 14. Effect of ambient temperature on preheating process.

maximum and minimum wall temperatures decrease from 547.6°C , 460.7°C – 399.6°C , 155.8°C , respectively, a decrease of 27.0% and 66.2%, respectively. As the wind speed increase, the preheating time increases. From 0 m/s to 4.5 m/s, t_{350} increases from 129 s to 229 s, an increase of 77.5%. Thus, the wind has a great impact on the preheating of the receiver. Under strong wind conditions, it is necessary to increase the heat flux for preheating.

4.1.3. Effect of wind direction on tube wall temperature

Fig. 12 shows the circumferential distributions of outer wall temperature under different wind directions when the preheating process is stable. The maximum wall temperature always appears at $\theta = 45^\circ$ at any wind direction. When the wind direction is 0° , 30° and 60° , the minimum wall temperature appears at $\theta = 180^\circ$, and it is at $\theta = 225^\circ$ (135°) when the wind direction is 90° . Different from the wind in the other three directions, the temperature on the windward side is still higher than the leeward side due to the same direction of the heat flux and wind direction ($\alpha = 90^\circ$). In addition, the minimum tube wall temperature cannot reach 230°C when the wind comes from the other three directions. As shown in Fig. 13, the wind of $\alpha = 60^\circ$ is the most unfavorable for the preheating process. Compared with the no-wind conditions, the maximum and minimum tube wall temperatures respectively decrease by 33.9% and 77.2% after the preheating is stable, and t_{350} increases from 129 s to 358 s, which increases by 177.5%.

4.1.4. Effect of ambient temperature on tube wall temperature

Fig. 14 shows the effect of ambient temperature on the preheating process. The maximum wall temperature, minimum wall temperature and preheating time are all linearly correlated with the ambient temperature. From -20°C to 40°C , the maximum wall temperature and the minimum wall temperature increase from 383.4°C , 119.1°C – 407.5°C , 173.7°C , respectively, an increase of 24.1°C , 54.6°C , respectively. The increase in minimum wall temperature is close to the increase in ambient temperature. Besides, t_{350} decreases from 303 s to 201 s, a decrease of 33.7%.

4.2. Thermal stress

4.2.1. Distribution and evolution of thermal stress

Fig. 15(a) shows the thermal stress evolutions of the outer wall at different circumferential positions under Case_3. Considering the symmetry, only the results of $\theta = 180^\circ - 360^\circ$ are presented. The

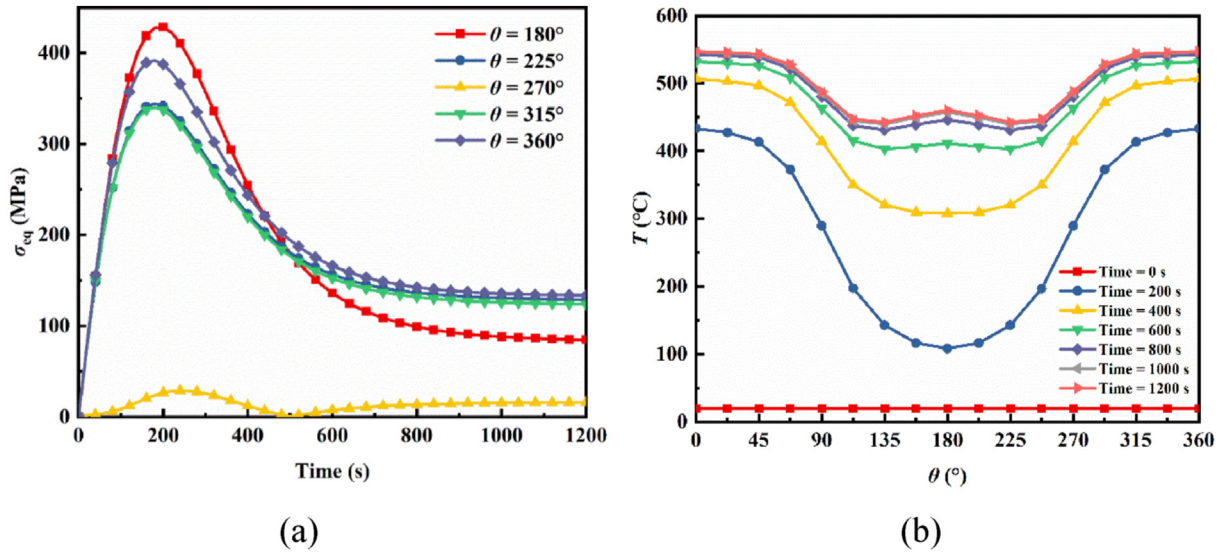


Fig. 15. (a) Thermal stress evolutions positions of the outer wall at different circumferential; (b) Circumferential temperature distributions at different time. ($q = 30 \text{ kW/m}^2$, $v = 0 \text{ m/s}$, $T_{\text{amb}} = 20^\circ \text{C}$).

equivalent thermal stress change at each circumferential position has the similar law. That is, it first rapidly increases to the peak value, then gradually decreases and finally reaches a stable value. The reason for the phenomenon is that the thermal stress is mainly affected by the circumferential temperature gradient. As shown in Fig. 15(b), after the start of preheating, the circumferential temperature gradient of the tube increases first and then decreases, which is similar to the evolution of the thermal stress. The maximum thermal stress appears at $\theta = 180^\circ$, which is 428.2 MPa. Due to the change of magnitude and direction of component stress σ_θ and σ_z , the peak thermal stress at $\theta = 270^\circ$ is the smallest in all circumferential positions [15].

4.2.2. Effect of parameter change on thermal stress

When there is no wind, the maximum thermal stress point of the tube wall is located at $\theta = 180^\circ$. With the change of wind speed and direction, the circumferential temperature distribution of the tube changes. As a result, the position of the maximum thermal stress is not fixed. When the wind comes from $\alpha = 0^\circ$, the maximum thermal stress is still at $\theta = 180^\circ$ under $v \leq 1.5 \text{ m/s}$, while it is at $\theta = 45^\circ$ When v increases further. When $\alpha = 90^\circ$, the maximum thermal stress point appears at $\theta = 180^\circ$. In other wind directions, it locates at $\theta = 45^\circ$. This is because the wind from $\alpha = 90^\circ$ is just loaded on the heated surface. Considering the uncertainty of the maximum thermal stress point, the maximum thermal stresses at $\theta = 45^\circ$ and $\theta = 180^\circ$ are used to analyze the influence of parameter change on thermal stress. As shown in Fig. 16, when the heat flux increases, the maximum thermal stress at $\theta = 45^\circ$ and $\theta = 180^\circ$ increases significantly, which respectively increases by 142.1% and 137.0% when the heat flux increases from 10 kW/m^2 to 40 kW/m^2 . And they respectively increase by 5.0% and decrease by 23.0% when the wind speed changes from 0 m/s to 4.5 m/s . When the wind direction is less than 90° , changing the wind direction has little effect on the maximum thermal stress at $\theta = 45^\circ$. When the wind direction increases from 0° to 60° , the maximum thermal stress at $\theta = 45^\circ$ and $\theta = 180^\circ$ decreases from 356.8 MPa, 329.9 MPa–355.0 MPa and 315.5 MPa respectively, with a change of -0.5% and 4.4% respectively. Under the wind direction $\alpha = 90^\circ$, the maximum thermal stress at $\theta = 45^\circ$ is less than that of $\theta = 180^\circ$. The maximum thermal stress at $\theta = 45^\circ$ and $\theta = 180^\circ$ is linearly related to the ambient temperature. When the ambient

temperature increases from -20°C to 40°C , the maximum thermal stress at $\theta = 45^\circ$ and $\theta = 180^\circ$ decreases by 10.4% and 10.0% respectively.

4.3. Effect of the uniformity of heat flux distribution on the preheating

For on-site receivers, it is difficult to ensure an absolutely uniform heat flux distribution during the preheating process. Thus, a discussion of preheating under non-uniform heat flux distribution is significant. Here, three heat flux distributions shown in Fig. 17 are employed. The average value of each heat flux distribution is equal, which is 30 kW/m^2 . Among them, q_1 is a uniform heat flux distribution while q_2 and q_3 are normally distributed. The peak heat fluxes of q_2 and q_3 are 45 kW/m^2 and 60 kW/m^2 , respectively. q_2 and q_3 can be expressed by $q = \frac{b}{a\sqrt{2\pi}} e^{-\frac{(z-7)^2}{2a^2}}$, where a , b are 4.101, 462585.715 for q_2 and 2.851, 428741.721 for q_3 .

Fig. 18(a) and Fig. 18(b) respectively present the axial distributions of outer wall temperature and outer wall thermal stress under the three heat flux distributions. Since the thermal performance of the receiver tube is mainly dependent on the heat flux during the preheating, the axial distributions of wall temperature and thermal stress are consistent with the corresponding heat flux distribution. Due to the higher peak heat flux, the maximum wall temperature and thermal stress under q_2 and q_3 are higher than those under q_1 . However, the circumferential positions of the maximum wall temperature and thermal stress are not affected by the uniformity of the heat flux distribution, and they are located at $\theta = 45^\circ$ and $\theta = 180^\circ$, respectively. The maximum wall temperatures and thermal stresses in the preheating process are 460.7°C , 562.3°C , 638.6°C and 365.2 MPa , 458.6 MPa , 537.9 MPa under q_1 , q_2 and q_3 , respectively. Based on that, when preheating the on-site receiver, a uniform heat flux distribution is required to avoid excessive wall temperature and thermal stress.

4.4. Tube wall temperature and thermal stress after salt circulating

Fig. 19 presents the outer wall temperature evolutions at different circumferential positions under different salt inlet temperatures after preheating is finished. The wall temperature is

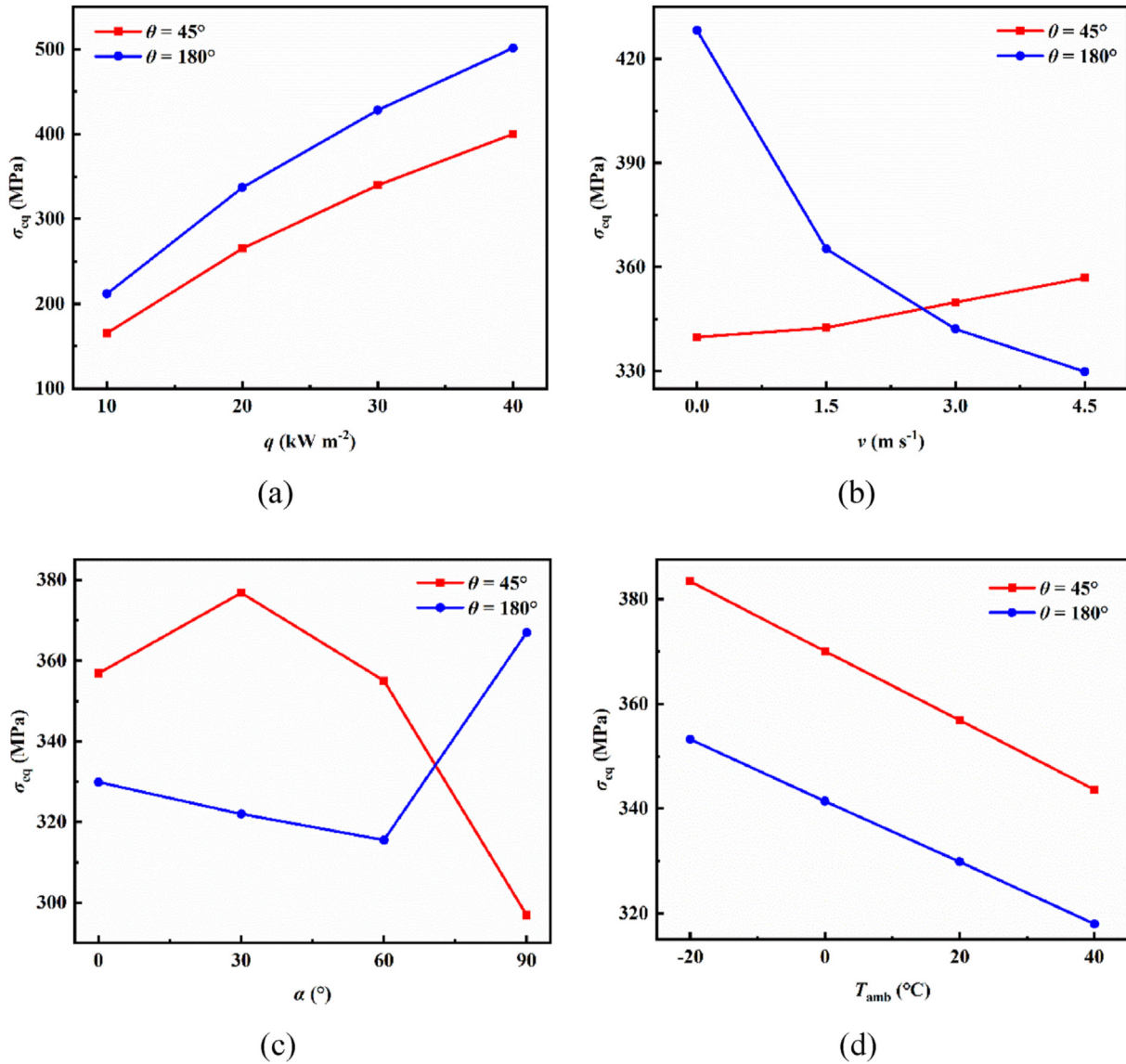


Fig. 16. Effect of parameter change on maximum thermal stress. (a) Heat flux; (b) Wind speed; (c) Wind direction; (d) Ambient temperature.

affected by both the molten salt and heat flux. Considering that the heat flux is small during the preheating process, the tube wall temperature after salt circulating is mainly determined by the molten salt. Thus, the wall temperature at each circumferential position changes to close to the salt inlet temperature after salt circulating, which leads to a significant decrease in the circumferential temperature gradient. Thus, as shown in Fig. 20, the thermal stress at the maximum stress point first decreases rapidly and then stabilizes after salt circulating. The reduction rates of thermal stress under different salt inlet temperatures are similar. The higher the salt inlet temperature is, the greater the stable thermal stress is. When the salt inlet temperature increases from 300°C to 500°C , the stable thermal stress increases from 22.7 MPa to 41.5 MPa.

Fig. 21 shows the outer wall temperature evolutions at different circumferential positions under different salt inlet mass flows after preheating is finished. When the salt inlet mass flow increases, the heat exchange between the molten salt and tube wall is enhanced. Naturally, the wall temperature decreases faster, and the stable temperature is lower. Fig. 22 presents the thermal stress evolution at the maximum thermal stress point. The effect of salt inlet mass

flow on the change of thermal stress is just opposite to that of salt inlet temperature, which mainly affects the reduction rate of thermal stress and has little effect on the stable thermal stress. From 1.0 kg/s to 4.0 kg/s, the thermal stress reduction rate within 200 s after salt circulating increases from 0.37 MPa/s to 0.41 MPa/s.

5. Conclusions

In this paper, the wall temperature and thermal stress distribution and evolution characteristics of molten salt tower receiver during preheating and salt filling in windy conditions are numerically studied by combining the FVM and two-dimensional thermoelastic method. In the preheating stage, the effects of heat flux, wind speed, wind direction, ambient temperature and uniformity of heat flux distribution are discussed. In the salt filling stage, the effects of salt inlet temperature and salt inlet mass flow are discussed. Some interesting conclusions are obtained as follows:

- (1) Under the no-wind conditions, the temperature rise rate of the tube front side is significantly higher than that of the

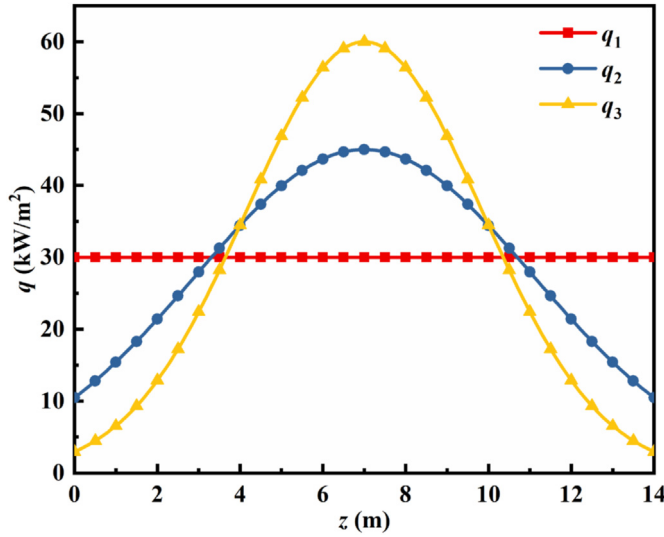
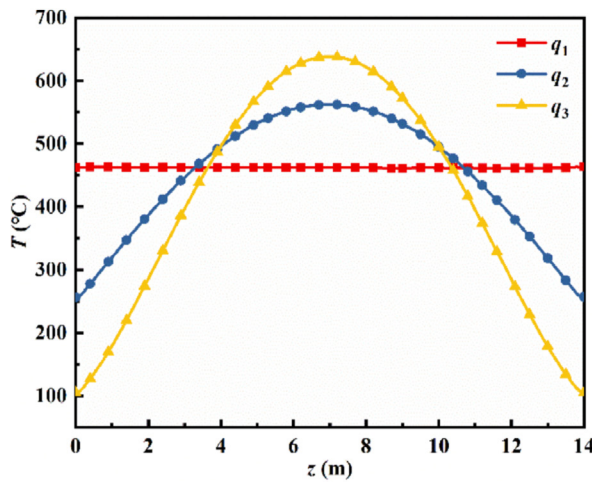


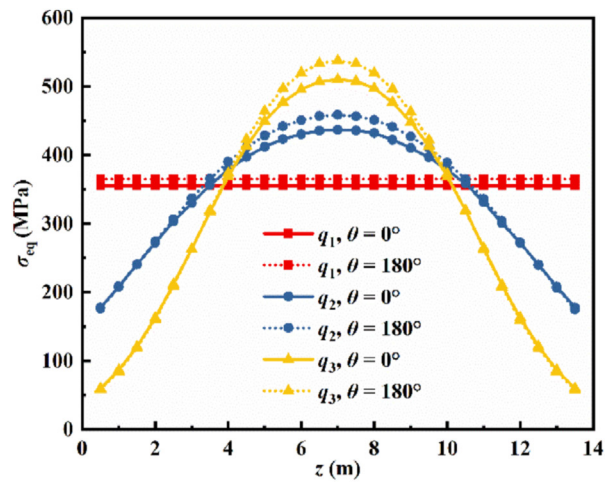
Fig. 17. The three heat flux distributions.

back side during the preheating process. The radial temperature difference of the tube wall does not exceed 2 °C during the entire preheating process, so the thermal stress is mainly determined by the circumferential temperature gradient. The increase of heat flux will significantly speed up the preheating process. When the heat flux increases from 10 kW/m² to 40 kW/m², t_{350} and t_{230} decrease by 95.0% and 69.9%, respectively. Moreover, when the heat flux is 10 kW/m², t_{350} is significantly larger than t_{230} , which means the receiver tube can be successfully preheated by directly loading a constant heat flux.

- (2) The circumferential distributions of tube wall temperature and thermal stress change with the wind speed and wind direction. The wind ($v = 4.5$ m/s, $\alpha = 60^\circ$) has the greatest impact on the preheating process. Compared with the no-wind conditions, the maximum and minimum wall temperatures decrease by 33.9% and 77.2%, respectively, and t_{350} increases by 177.5%. The maximum wall temperature, minimum wall temperature and preheating time are all linearly related to the ambient temperature. The increment of minimum wall temperature is close to that of ambient temperature.
- (3) The thermal stress evolution at each circumferential position has the same law. That is, it first rapidly increases to the peak value, then gradually decreases and finally reaches a stable value. With the increase of heat flux, wind speed or ambient temperature, the maximum thermal stress at $\theta = 45^\circ$ increases, increases, and decreases, respectively. And the maximum thermal stress at $\theta = 180^\circ$ increases, decreases, and decreases, respectively. When the wind direction is smaller than 90° , changing the wind direction has little effect on the maximum thermal stress. When the wind direction increases from 0° to 60° , the maximum thermal stress at $\theta = 45^\circ$ and $\theta = 180^\circ$ decreases by 0.5% and 4.4%, respectively.
- (4) During the preheating, the axial distribution of the tube wall temperature and thermal stress is consistent with the loaded heat flux distribution, and the uneven heat flux distribution will cause a significant increase in the maximum wall temperature and maximum thermal stress.
- (5) During the salt filling process, the wall temperature of each circumferential position quickly approaches the salt inlet temperature, and the thermal stress drops rapidly. The salt inlet temperature mainly affects the stable thermal stress, while has little effect on the thermal stress reduction rate. The salt inlet mass flow is just the opposite.



(a)



(b)

Fig. 18. Axial distribution of outer wall temperature and outer wall thermal stress under three heat flux distributions. (a) The axial wall temperature distribution at $\theta = 45^\circ$ when the receiver tube is preheated to a stable state; (b) The axial thermal stress distribution when the thermal stress reaches the maximum. ($v = 1.5$ m/s, $\alpha = 0^\circ$, $T_{amb} = 20^\circ\text{C}$).

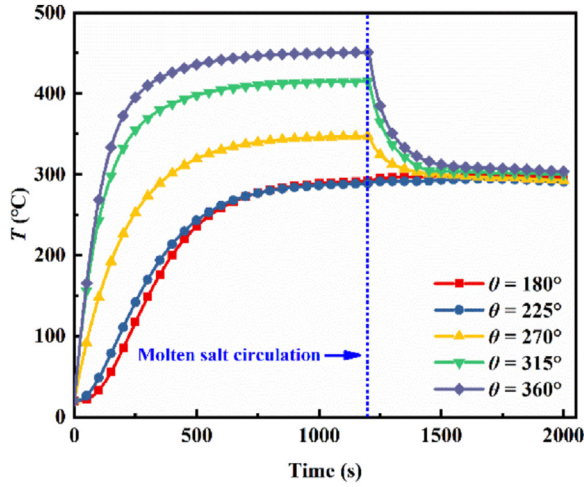
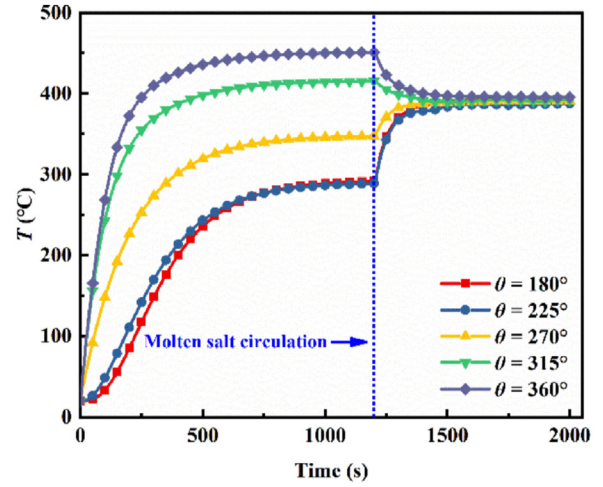
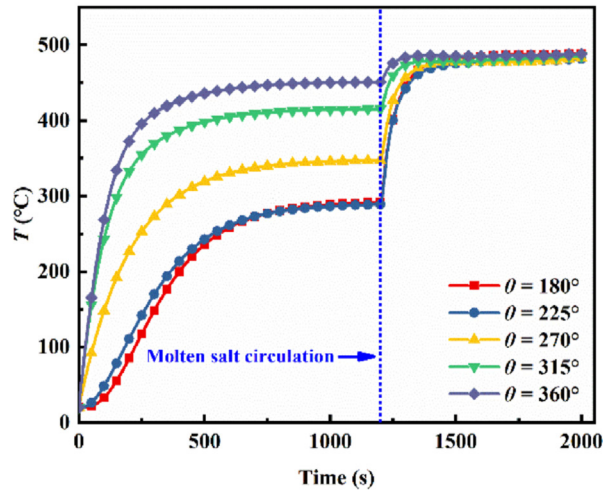
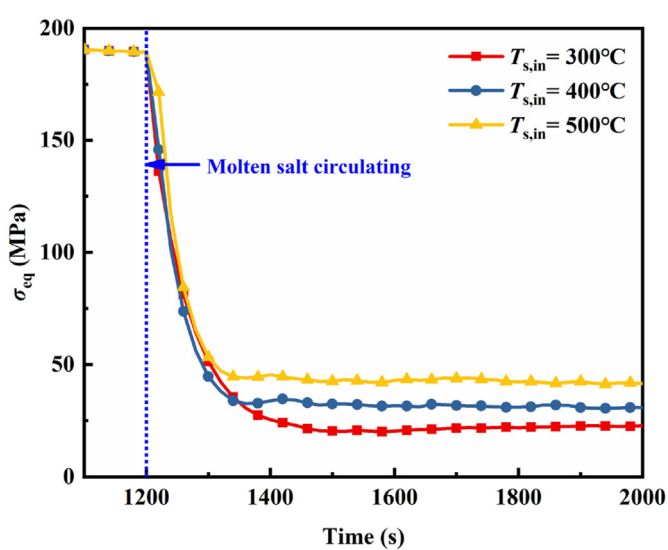
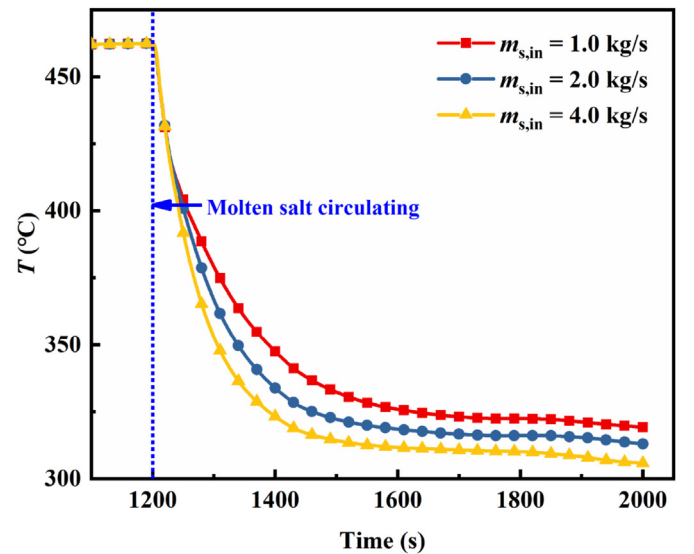
(a) $T_{s,in} = 300\text{ }^{\circ}\text{C}$ (b) $T_{s,in} = 400\text{ }^{\circ}\text{C}$ (c) $T_{s,in} = 500\text{ }^{\circ}\text{C}$

Fig. 19. Outer wall temperature evolutions at different circumferential positions under different salt inlet temperatures.

Fig. 20. Thermal stress evolutions of the maximum thermal stress point ($\theta = 180^{\circ}$) under different salt inlet temperatures.Fig. 21. Outer wall temperature evolutions of the maximum wall temperature point ($\theta = 45^{\circ}$) under different salt inlet mass flows.

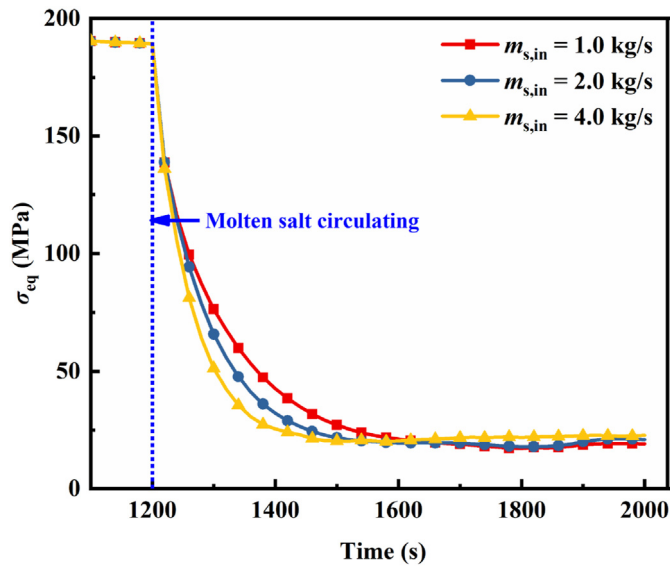


Fig. 22. Thermal stress evolutions of the maximum thermal stress point ($\theta = 180^\circ$) under different salt mass flows.

Credit author statement

Yuhang Zuo: Conceptualization, Methodology, Validation, Formal analysis, Investigation, Writing - original draft, Writing - review & editing. **Yawei Li:** Conceptualization, Methodology, Investigation. **Hao Zhou:** Conceptualization, Methodology, Resources, Supervision, Project administration.

Declaration of competing interest

The authors declare that they have no known competing financial interests or personal relationships that could have appeared to influence the work reported in this paper.

Acknowledgement

This research did not receive any specific grant from funding agencies in the public, commercial, or not-for-profit sectors.

Nomenclature

Greek symbols

α	wind direction ($^\circ$)
ν	Poisson's ratio
θ	cylindrical coordinate (rad)
λ	linear thermal expansion coefficient (K^{-1})
σ	stress (Pa)
Δ	difference

Roman symbols

B, D	Fourier coefficients
E	Young's modulus (Pa)
K	geometric thermal stress term (K)
m	mass flow (kg/s)
q	heat flux (W/m^2)
r	radial coordinate (m)
T	temperature (K)
\bar{T}	mean temperature (K)
t	time (s)

v	Wind speed (m/s)
z	axial coordinate (m)

Abbreviations

CSP	concentrating solar power
DNI	direct normal irradiation
FVM	finite volume method

Subscripts

amb	ambient
eq	equivalent
s	salt
in	inlet
i	inner wall
o	outer wall
r	radial component
z	axial component
θ	circumferential component

References

- [1] González-Roubaud E, Pérez-Osorio D, Prieto C. Review of commercial thermal energy storage in concentrated solar power plants: steam vs. molten salts. *Renew Sustain Energy Rev* 2017;80:133–48. <https://doi.org/10.1016/j.rser.2017.05.084>.
- [2] Kolb GJ, Ho CK, Mancini TR, Gary JA. Power tower technology roadmap and cost reduction plan. *Conc Sol Power Data Dir an Emerg Sol Technol* 2012: 223–50.
- [3] Yu Q, Fu P, Yang Y, Qiao J, Wang Z, Zhang Q. Modeling and parametric study of molten salt receiver of concentrating solar power tower plant. *Energy* 2020;200. <https://doi.org/10.1016/j.energy.2020.117505>.
- [4] Albarbar A, Arar A. Performance assessment and improvement of central receivers used for solar thermal plants. *Energies* 2019;12. <https://doi.org/10.3390/en12163079>.
- [5] Xu L, Stein W, Kim JS, Too YCS, Guo M, Wang Z. Transient numerical model for the thermal performance of the solar receiver. *Appl Therm Eng* 2018;141: 1035–47. <https://doi.org/10.1016/j.applthermaleng.2018.05.112>.
- [6] Qaisrani MA, Fang J, Jin Y, Wan Z, Tu N, Khalid M, et al. Thermal losses evaluation of an external rectangular receiver in a windy environment. *Sol Energy* 2019;184:281–91. <https://doi.org/10.1016/j.solener.2019.03.103>.
- [7] Cagnoli M, de la Calle A, Pye J, Savoldi L, Zanino R. A CFD-supported dynamic system-level model of a sodium-cooled billboard-type receiver for central tower CSP applications. *Sol Energy* 2019;177:576–94. <https://doi.org/10.1016/j.solener.2018.11.031>.
- [8] Rodríguez-Sánchez MR, Soria-Verdugo A, Almendros-Ibáñez JA, Acosta-Iborra A, Santana D. Thermal design guidelines of solar power towers. *Appl Therm Eng* 2014;63:428–38. <https://doi.org/10.1016/j.applthermaleng.2013.11.014>.
- [9] Cantone M, Cagnoli M, Fernandez Reche J, Savoldi L. One-side heating test and modeling of tubular receivers equipped with turbulence promoters for solar tower applications. *Appl Energy* 2020;277:115519. <https://doi.org/10.1016/j.apenergy.2020.115519>.
- [10] Du BC, He YL, Zheng ZJ, Cheng ZD. Analysis of thermal stress and fatigue fracture for the solar tower molten salt receiver. *Appl Therm Eng* 2016;99: 741–50. <https://doi.org/10.1016/j.applthermaleng.2016.01.101>.
- [11] Qaisrani MA, Wei J, Fang J, Jin Y, Wan Z, Khalid M. Heat losses and thermal stresses of an external cylindrical water/steam solar tower receiver. *Appl Therm Eng* 2019;163:114241. <https://doi.org/10.1016/j.applthermaleng.2019.114241>.
- [12] Zhou H, Li Y, Zuo Y, Zhou M, Fang W, Zhu Y. Thermal performance and thermal stress analysis of a 600 MWth solar cylinder external receiver. *Renew Energy* 2021;164:331–45. <https://doi.org/10.1016/j.renene.2020.09.073>.
- [13] Wang F, Shuai Y, Yuan Y, Liu B. Effects of material selection on the thermal stresses of tube receiver under concentrated solar irradiation. *Mater Des* 2012;33:284–91. <https://doi.org/10.1016/j.matdes.2011.07.048>.
- [14] Logie WR, Pye JD, Coventry J. Thermoelastic stress in concentrating solar receiver tubes: a retrospect on stress analysis methodology, and comparison of salt and sodium. *Sol Energy* 2018;160:368–79. <https://doi.org/10.1016/j.solener.2017.12.003>.
- [15] Montoya A, Rodríguez-Sánchez MR, López-Puente J, Santana D. Numerical model of solar external receiver tubes: influence of mechanical boundary conditions and temperature variation in thermoelastic stresses. *Sol Energy* 2018;174:912–22. <https://doi.org/10.1016/j.solener.2018.09.068>.
- [16] Bonk A, Sau S, Uranga N, Hernaiz M, Bauer T. Advanced heat transfer fluids for direct molten salt line-focusing CSP plants. *Prog Energy Combust Sci* 2018;67: 69–87. <https://doi.org/10.1016/j.pecs.2018.02.002>.
- [17] Vant-Hull LL. The role of "allowable flux density" in the design and operation of molten-salt solar central receivers. *J Sol Energy Eng Trans ASME* 2002;124:

- 165–9. <https://doi.org/10.1115/1.1464124>.
- [18] Price H, Mehos M, Kearney D, Cable R, Kelly B, Kolb G, et al. Concentrating solar power best practices. *Conc Sol Power Technol* 2021;725–57. <https://doi.org/10.1016/b978-0-12-819970-1.00020-7>.
- [19] Lu J, Ding J. Dynamical and thermal performance of molten salt pipe during filling process. *Int J Heat Mass Tran* 2009;52:3576–84. <https://doi.org/10.1016/j.ijheatmasstransfer.2009.03.005>.
- [20] Lu J, Ding J, Yang J. Filling dynamics and phase change of molten salt in cold receiver pipe during initial pumping process. *Int J Heat Mass Tran* 2013;64:98–107. <https://doi.org/10.1016/j.ijheatmasstransfer.2013.04.021>.
- [21] Fernández-Torrijos M, Sobrino C, Almendros-Ibáñez JA, Marugán-Cruz C, Santana D. Inverse heat problem of determining unknown surface heat flux in a molten salt loop. *Int J Heat Mass Tran* 2019;139:503–16. <https://doi.org/10.1016/j.ijheatmasstransfer.2019.05.002>.
- [22] Fernández-Torrijos M, Sobrino C, Marugán-Cruz C, Santana D. Experimental and numerical study of the heat transfer process during the startup of molten salt tower receivers. *Appl Therm Eng* 2020;178:115528. <https://doi.org/10.1016/j.applthermaleng.2020.115528>.
- [23] Pérez-Álvarez R, González-Gómez PÁ, Acosta-Iborra A, Santana D. Thermal stress and fatigue damage of central receiver tubes during their preheating. *Appl Therm Eng* 2021;195. <https://doi.org/10.1016/j.applthermaleng.2021.117115>.
- [24] Wan Z, Fang J, Tu N, Wei J, Qaisrani MA. Numerical study on thermal stress and cold startup induced thermal fatigue of a water/steam cavity receiver in concentrated solar power (CSP) plants. *Sol Energy* 2018;170:430–41. <https://doi.org/10.1016/j.solener.2018.05.087>.
- [25] El Hefni B. Detailed dynamic model for the gravity drainage of a tower solar receiver, with ThermoSysPro library - time needed to completely drain the receiver and salt temperature as a function of the ambient conditions. *AIP Conf Proc* 2019;2126. <https://doi.org/10.1063/1.5117531>.
- [26] Yang L, Ling X, Peng H, Duan LF, Chen X. Starting characteristics of a novel high temperature flat heat pipe receiver in solar power tower plant based of "Flat-front" Startup model. *Energy* 2019;183:936–45. <https://doi.org/10.1016/j.energy.2019.07.007>.
- [27] Rodríguez-Sánchez MR, Marugán-Cruz C, Acosta-Iborra A, Santana D. Comparison of simplified heat transfer models and CFD simulations for molten salt external receiver. *Appl Therm Eng* 2014;73:993–1005. <https://doi.org/10.1016/j.applthermaleng.2014.08.072>.
- [28] Marugán-Cruz C, Flores O, Santana D, García-Villalba M. Heat transfer and thermal stresses in a circular tube with a non-uniform heat flux. *Int J Heat Mass Tran* 2016;96:256–66. <https://doi.org/10.1016/j.ijheatmasstransfer.2016.01.035>.
- [29] Zhou H, Li Y, Zhou M, Liu D, Fang W. Numerical simulation of a lab-scale molten-salt external solar receiver and its experimental validation. *J Energy Eng* 2021;147:4020074.
- [30] Zhou H, Li Y, Zhu Y, Fang W, Cen K. Experimental and numerical evaluation of a lab-scale external solar receiver. *J Renew Sustain Energy* 2020;12:43705.